Separation and Purification Technology 136 (2014) 296–302

Contents lists available at ScienceDirect

Separation and Purification Technology

journal homepage: www.elsevier.com/locate/seppur

Profiling vertical distribution of scalants in RO membranes by LA-ICP-MS and fouling models

Justin Chun-Te Lin [a], Tsinghai Wang [b], Yu-Hsuan Ku [b], Yi-Kong Hsieh [b], Chu-Fang Wang [b,*]

[a] Disaster Prevention and Water Environmental Research Center, National Chiao Tung University, Hsinchu 300, Taiwan
[b] Department of Biomedical Engineering and Environmental Sciences, National Tsing Hua University, Hsinchu 300, Taiwan

ARTICLE INFO

Article history:
Received 10 June 2014
Received in revised form 16 August 2014
Accepted 18 August 2014
Available online 27 August 2014

Keywords:
LA-ICP-MS
Membrane scaling
Vertical distribution
Spot mode
Reverse osmosis

ABSTRACT

The vertical distribution of scalants as a result of 24 h of filtration of simulated low-level radioactive liquid waste in the reverse osmosis (RO) membranes was characterized by means of laser ablation inductively coupled plasma mass spectrometry (LA-ICP-MS). Our results suggested that the development of scalants is associated with the formation of metal hydroxide colloids, while these colloids might penetrate relatively deeper into the membrane under the acid environment than under the alkaline environment. Fitting with a two-phase fouling Hermia's model suggested that the development of cake-like scalants in the first 5 h under alkaline environment is responsible for hindering the assess of metal hydroxides into the membrane so that they would not penetrate as deep as they do under the acid environment.

1. Introduction

Scaling and fouling are two frequently observed problems in membrane-based treatment processes [1–7]. Recently, membrane-based processing technologies are increasingly adopted by the nuclear communities for the low-level radioactive liquid waste (LLRW) treatment [8–12]. This arises the importance of gathering better knowledge regarding the scalant development during the filtration of LLRW because it helps to keep the relatively high removal efficiency and produce less amount of waste. Various surface analysis techniques, including scanning electron microscopy (SEM) with energy-dispersive X-ray spectroscopy (EDX), transmission electron microscopy (TEM), X-ray diffraction (XRD), confocal laser microscopy (CLSM), and atomic force microscopy (AFM) and other in situ monitoring techniques have been applied to characterize the membrane scaling [13,14]. Recently, an alternative surface analysis technique, the laser ablation inductively coupled plasma mass spectrometry (LA-ICP-MS), has been demonstrated capable of quantitatively analyzing the element composition of a versatile of solid samples with a good sensitivity down to part-per-million level [15–21]. By adopting the spot mode together with appropriate operation conditions, the depth profiles of analytes could be visualized with a resolution down to the micrometer scale as we are demonstrating in this study.

Apart from the techniques that have been applied for scalant characterization, a number of researchers were also attempting to modeling the permeate flux variation with an appropriate physical model [22–28]. One of the most successful models used to interpret the fouling mechanisms under constant pressure is the Hermia's model [28]. This model describes four fouling mechanisms that account for the observed flux variation: (i) complete blocking, (ii) intermediate blocking, (iii) standard blocking, and (iv) cake formation. The general term describing these fouling mechanisms is shown as follows:

$$\frac{d^2t}{dV^2} = k\left(\frac{dt}{dV}\right)^n \quad \text{or} \quad \frac{dJ_v}{dt} = -kJ_v(J_v)^{2-n} \tag{1}$$

where V is the cumulative volume of filtration, t is the operation time, and k is a parameter that varies with n, while the n value is given depending on which kind of blocking is taking place.

(i) Cake formation model, at which $n = 0$ (Eq. (2)). It assumes that fouling development is due to the cake formation on the membrane surface. In this process, foulants deposit on the particles that already block the pores, and this results in cake formation.

$$\frac{dJ_v}{dt} = -k_A(J_v - J^*) \tag{2}$$

* Corresponding author. Tel.: +886 3 5715131x34222; fax: +886 3 5718649.
E-mail address: cfwang@mx.nthu.edu.tw (C.-F. Wang).

http://dx.doi.org/10.1016/j.seppur.2014.08.018
1383-5866/

Nomenclature

J	permeate flux (m s^{-1})	K_{cf}	cake formation parameter (s m^{-2})
J_0	initial permeate flux (m s^{-1})	K_{pc}	pore constriction parameter ($s^{-1/2}$)
t	time (s)	K_{ib}	intermediate blocking parameter (m^{-1})
A	membrane area (m^2)	K_{cb}	complete blocking parameter (s^{-1})
C	suspended solid concentration (g/L)	ΔP	trans-membrane pressure (Pa)
e	active layer thickness (m)	α	specific cake resistance (m/kg)
h	deposit height (m)	μ_p	permeate viscosity (Pa s)
k	constant kinetics parameter	ρ_s	density (kg/m^3)

(ii) Intermediate blocking model, at which $n = 1$ (Eq. (3)); this model is based on the probability of a pore being blocked by particles near the membrane surface. A single particle can precipitate on others to form multi-layers, and this process can directly block some membrane pores, resulting in an increase in the cake thickness.

$$\frac{dJ_v}{dt} = -k_B J_V^{0.5}(J_v - J^*) \quad (3)$$

(iii) Pore constriction or standard blocking model, at which $n = 1.5$ (Eq. (4)); this model is based on a decrease in membrane pore diameter due to adherence of particles on the pore wall. This usually happens when the size of colloids are smaller than that of the membrane pore size.

$$\frac{dJ_v}{dt} = -k_C J_v(J_v - J^*) \quad (4)$$

(iv) Complete pore blocking model, at which $n = 2.0$ (Eq. (5)); this model assumes that each particle settling on the membrane surface will block a pore. This occurs when the size of foulants is similar to the membrane pore size, which results in a reduction in the number of open pores without particle deposits on the membrane surface in the first place.

$$\frac{dJ_v}{dt} = -k_D J_V^2(J_v - J^*) \quad (5)$$

In this study, we first adopted means of LA-ICP-MS to characterize the vertical distribution of membrane scaling. Experimental results were further fitted by Hermia's model to reveal the blocking mechanism behind. Although Hermia's model was built based the rigid spheres blocking the pores of membrane, it is still able to qualitatively insight into the fouling mechanism caused by colloids during the RO filtration. Together with the thermodynamic-basis aqueous chemistry calculation, we demonstrated herein the scalants developed during the RO filtration of simulated low-level radioactive liquid waste was mainly resulted from the formation of metal hydroxide colloids. The vertical distribution of these scalants was locating at first few micrometers beneath the membrane surface and was strongly dependent on the filtration pH environment. Relevant information would be helpful to better understand the fouling behaviors of membrane-basis treatment systems.

Table 1
Operation conditions in the spot mode of laser ablation.

Parameters	Setting
Wavelength	213 nm
Repetition rate	1 Hz
Scanning speed	–
Durations	1, 5, 10, 20, 40, 60 s
Focused spot size	30 μm
Output energy	70%
Laser energy	4.17 J/cm^2 (0.03 mJ)
Line spacing	–
Carrier gas (Ar)	1.01 L min^{-1}

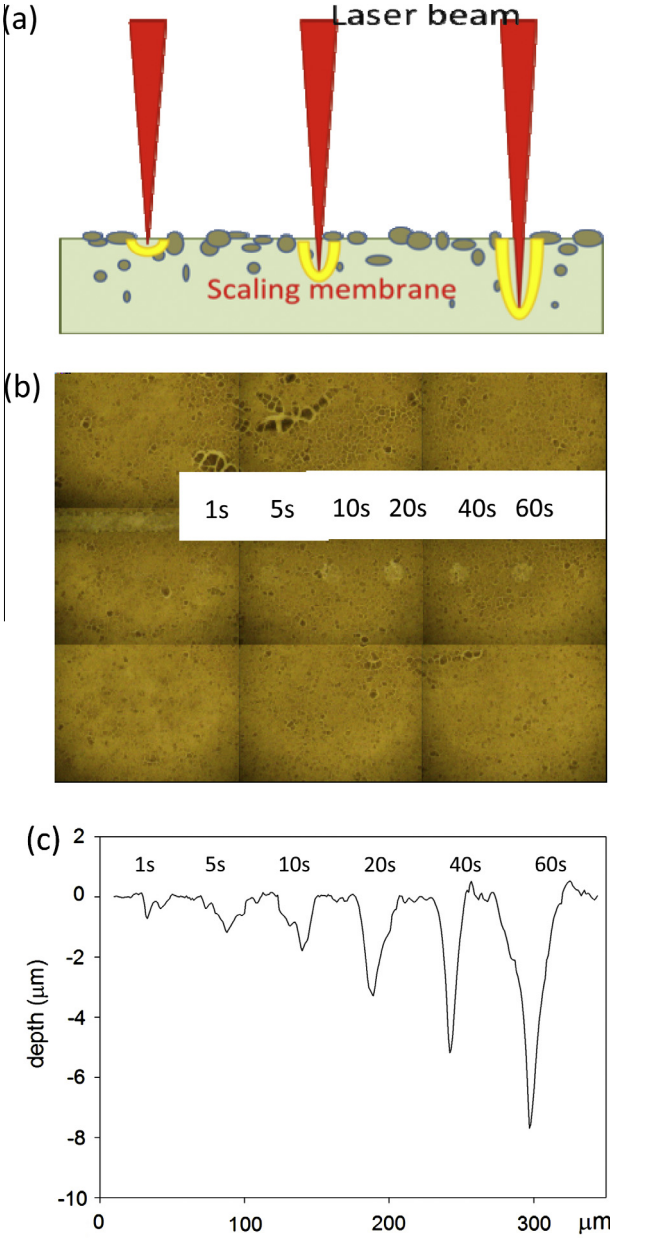

Fig. 1. (a) The illustration of laser beam ablation on membrane surface with various dwelling times; (b) the photograph showing six craters created by laser ablation with different dwelling times; (c) depth profile analysis of each crater by the alpha-step profilometer.

2. Materials and methods

2.1. Chemicals and membranes

Chemicals used in this study included: sodium hydroxide, cesium chloride, calcium chloride dihydrate, copper(II) chloride dihydrate, magnesium chloride hexahydrate, zinc(II) chloride, nitric acid (65%, extra pure), silver, and antimony ICP standard solution (1000 mg L^{-1}, diluted in nitric acid) were all analytical grade and purchased from Merck. Chromium(II) chloride hexahydrate and manganese(II) chloride 4-hydrate were from J.T. Baker; iron(III) chloride hexahydrate (purity ≧ 99%) and methylene blue ($C_{16}H_{18}ClN_3S{\cdot}3H_2O$, reagent grade) were obtained from Sigma–Aldrich. Cobalt(II) chloride hexahydrate (ACS, 98–102%) was obtained from Alfa Aesar. Deionized water (Milli-Q, Millipore, >18 MΩ cm^{-1}) was used for feed solutions preparation and flushing. Since no other oxidation and reduction reagents were added in the feed solution, it is assumed that the oxidation states of these transition elements should be their dissolved cationic species. Flat-sheet polyamide RO membranes (AD™, GE-Osmonics Co., USA) were chosen to observe the formation of inorganic scale in this study. Reported rejection rates by the GE-Osmonics are 99.2–99.5% in sodium chloride solution with the operation conditions covering pH 4–11.

2.2. Feed compositions and filtration protocol

All experiments were conducted with our homemade filtration system [21]. It contained three channels in parallel that was capable of placing three individual RO membranes at the same time. This feature allowed triplicate experiments performed simultaneously.

Table 2
Selected reactions and formation constants for Co^{2+}, Fe^{3+}, Cu^{2+} and Zn^{2+} species.

Reactions	Log K[a]
$H_2O = H^+ + OH^-$	−13.99
Co^{2+}	
$Co^{2+} + 2H_2O = Co(OH)_2\ aq + 2H^+$	−18.79
$Co^{2+} + 4H_2O = Co(OH)_4^{2-} + 4H^+$	−46.28
$Co^{2+} + 3H_2O = Co(OH)_3^- + 3H^+$	−31.39
$4Co^{2+} + 4H_2O = Co_4(OH)_4^{4+} + 4H^+$	−30.48
$2Co^{2+} + H_2O = Co_2(OH)^{3+} + H^+$	−10.99
$Co^{2+} + 2H_2O = CoOOH^- + 3H^+$	−32.09
$Co^{2+} + H_2O = CoOH^+ + H^+$	−9.69
Fe^{3+}	
$Fe^{3+} + H_2O = FeOH^{2+} + H^+$	−2.18
$Fe^{3+} + 2H_2O = Fe(OH)_2^+ + 2H^+$	−4.59
$2Fe^{3+} + 2H_2O = Fe_2(OH)_2^{4+} + 2H^+$	−2.85
$Fe^{3+} + 3H_2O = Fe(OH)_3\ aq + 3H^+$	−12.56
$Fe^{3+} + 4H_2O = Fe(OH)_4^- + 4H^+$	−21.58
$3Fe^{3+} + 4H_2O = Fe_3(OH)_4^{5+} + 4H^+$	−6.29
Hematite (Fe_2O_3) precipitate	0.87
Cu^{2+}	
$Cu^{2+} + 2H_2O = Cu_2(OH)_2^{2+} + 2H^+$	−10.59
$Cu^{2+} + 3H_2O = Cu(OH)_3^- + 3H^+$	−26.88
$Cu^{2+} + 4H_2O = Cu(OH)_4^{2-} + 4H^+$	−39.98
$Cu^{2+} + H_2O = CuOH^+ + H^+$	−7.49
$Cu^{2+} + 2H_2O = Cu(OH)_2\ aq + 2H^+$	−16.19
Tenorite (CuO) precipitate	−7.73
Zn^{2+}	
$Zn^{2+} + 4H_2O = Zn(OH)_4^{2-} + 4H^+$	−13.99
$Zn^{2+} + 3H_2O = Zn(OH)_3^- + 3H^+$	−40.48
$Zn^{2+} + H_2O = ZnOH^+ + H^+$	−8.99
$Zn^{2+} + 2H_2O = Zn(OH)_2\ aq + 2H^+$	−17.79
ZnO precipitate	−11.31

[a] These values were adopted from the built-in thermodynamic database of MINEQL, which incorporates a thermodynamic database containing the entire USEPA MINTEQA2 database plus data and this feature allows all calculations compatible with EPA specifications [30].

The effective filtration area was 23.6 cm^2 (2.65 cm × 8.9 cm), and experiments were conducted at 28 ± 0.5 °C and 30 bars (435 psi). The composition of feed solution selected herein was based on the reported composition of low-level radioactive liquid waste [12]. The pH of as-prepared feed solution was carefully kept at pH 4 before filtration experiments to prevent the formation of metal hydroxide colloids. Filtration experiments were conducted at pH 4 and pH 9, while the depth profile analysis was executed with the

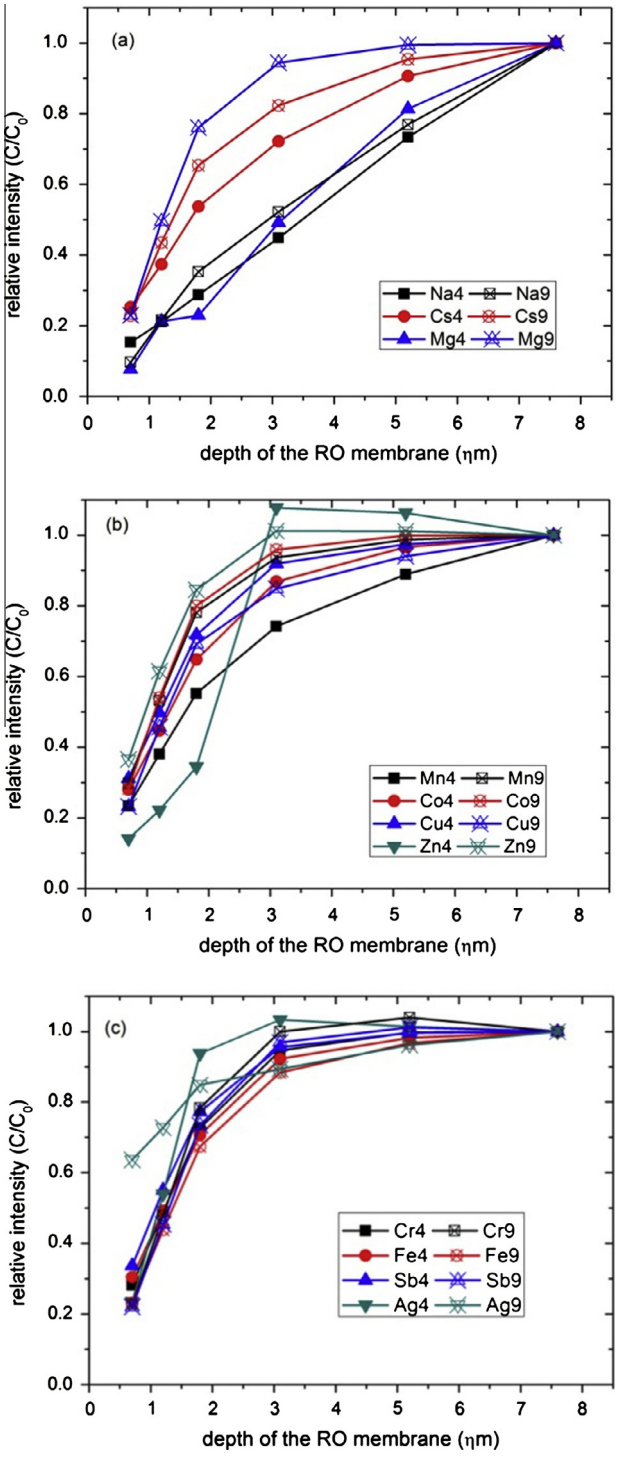

Fig. 2. The profiles of element distribution of scalants in RO membranes: (a) Mg, Cs, and Na at pH 4 and pH 9; (b) Co, Mn, Cu, and Zn at pH 4 and pH 9; (c) Cr, Fe, Sb, and Ag at pH 4 and pH 9, respectively. Values shown in the end of each element refer to the pH condition where the filtration experiments were conducted. The data set selected herein was the one closest to the average values.

RO membrane collected in both conditions. The concentrations (in parentheses) of individual element in the feed solution were Na (1337 ppm; 58.13 mM), Mg (7.1 ppm; 0.29 mM), Cs (297 ppm; 2.23 mM), Mn (12.8 ppm; 0.23 mM), Co (277 ppm; 4.69 mM), Cu (14.3 ppm; 0.22 mM), Zn (10.1 ppm; 0.15 mM), Ag (4.6 ppm; 0.02 mM), Cr (11.7 ppm; 0.23 mM), Fe (22.9 ppm; 0.4 mM), and Sb (11.9 ppm; 0.10 mM), respectively. Meanwhile, the concentration of chloride was determined as 1127 ppm (31.75 mM) by ion chromatography.

The silt density index (SDI) of the feed solutions was tested as 1.6, which means it is could be used straightforwardly for RO and NF filtrations. The RO filtration experiments were carried out for 24 h, and the permeates and bypass flows were recycled back to the feed tank. After 24 h of filtration, the scaled membranes were air-dried for 48 h and then mounted on glass slides before LA-ICP-MS and alpha-step profilometer analysis.

2.3. Analytical methods

A laser ablation system (UP-213, New Wave Research Inc., Fremont, CA, USA) was used for sample ablation prior to elemental analysis by inductively coupled plasma mass spectrometry (ICP-MS, 7500a, Agilent, USA). The spot mode was used to investigate the depth profile of scalant distribution in the RO membranes. The operation conditions were listed in Table 1. For depth profile analysis, laser beam was constantly ablating the same position with different dwelling times covering from 1 to 60 s (Fig. 1a and b). An α-step profilometer (Dektak 150, Veeco) was used to measure the depth of the individual craters produced by laser ablation (Fig. 1c). The read signal intensities of each elements were converted and plotted on a bar diagram by using MATrix LABoratory (MATLAB®) software. For quantitative analysis, individual calibration curves of studied elements (Na, Mg, Cr, Mn, Fe, Co, Cu, Zn, Ag, Sb, Cs) were established by dropping one microliter of ICP standard solution onto a virgin RO membrane to form a droplet. Methylene blue was added into all standard solutions, which is particularly benefit for laser beam alignment. For quality control, there were at least 10 spots over three RO membranes studied for each condition. The data set presented herein was the one closest to the average values.

2.4. Model simulation and parameter fitting and thermodynamic-based aqueous chemistry calculation

Experiment data were further fitted by using Gnuplot program to determine the parameters of best-fitting curves based on the highest correlation coefficients (R^2) [29]. The variations of normalized flux (J/J_0) against elapsing time were fitted with each fouling model as described in Eqs. (2)–(5) to determine the corresponding K value. The thermodynamic-based aqueous chemistry calculation was conducted by using an MINEQL+4.6 version, which is a chemical equilibrium modeling system developed to solve mass balance expressions using equilibrium constants, combining the database of WATEQ3 and the numerical structure of MINEQL [30]. All the considered chemical reactions were presented in Table 2.

3. Results and discussions

3.1. Vertical distributions of scalants in the RO membranes

Considering that the concentration between studied elements was spanning up to three orders of magnitude, we thus normalized the read intensity of each element in order to process further quantitative interpretation. As shown in Fig. 2, two distinct patterns are

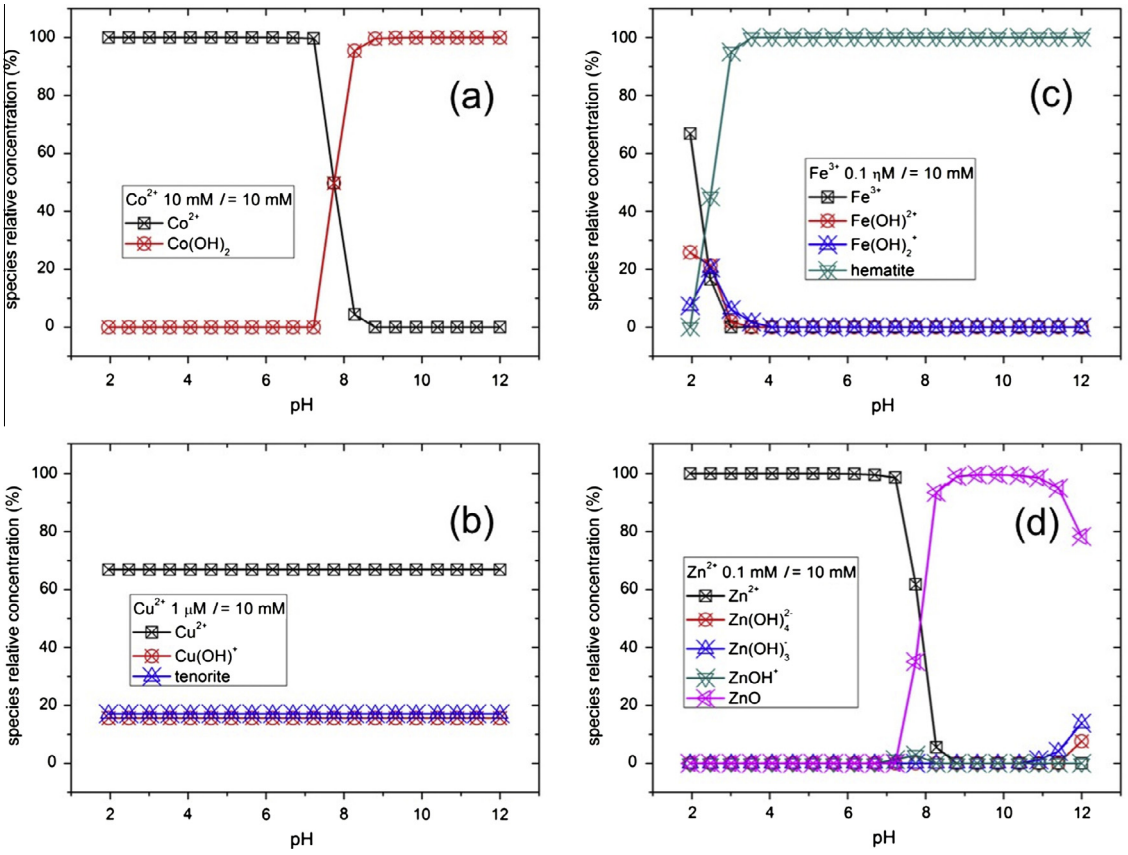

Fig. 3. The simulation results of species distribution in different pH environments (a) Co^{2+} (with initial concentration of 10 mM); (b) Cu^{2+} (with initial concentration of 1 μM); (c) Fe^{3+} (with initial concentration of 0.1 μM); (d) Zn^{2+} (with initial concentration of 0.1 mM). The ionic strength, I, was assumed 10 mM.

noted; one possesses a linear response (Type I) at which the intensity increases proportionally with increasing depth, while the other exhibits a plateau feature (Type II) that the intensity would not significantly increase furthermore as the ablation gets deeper. To our best knowledge, this is the first time that one is able to visualize the vertical distributions of multi-element (up to 11 elements) in the RO membranes. By carefully comparing the correlation and distribution of these elements, one would have a better knowledge regarding the element composition of scalants developing in the RO membrane.

In the case of Type I pattern, the read intensity increases proportionally with increasing depth, suggesting that the element distribution is rather homogeneous along the depth of the membrane. This means elements that behave in this manner (Na, Cs at pH 4 and Na at pH 9) would not be effectively rejected by the RO membrane filtration. In other words, these elements could readily penetrate through the RO membrane. In contrary, elements exhibiting a plateau feature (Type II) suggest that they are likely to be effectively removed from the feed solution in the end of filtration. As pH rose, most elements in Fig. 2a seemed to concentrate at the first 3 micrometers beneath the RO membrane. Similar transitions are also observed in Fig. 2b and c. This might be explained by the formation of metal hydroxide colloids and afterward interactions between ions and metal oxide colloids. Based upon thermodynamic-based aqueous chemistry calculation, in a low ionic strength environment like the current presented one, the majority of studied elements (expect Na and Cs) would form metal hydroxide colloids in the feed solution as the pH rises to the alkaline environment (Fig. 3). Particularly, some of them even possess a concentration that is much greater than their corresponding threshold concentrations (the concentration at which the formation of metal hydroxide becomes significant). In other words, from the point of view of thermodynamics, the formation of metal hydroxide colloids is favorable in our studied system and these metal hydroxide colloids are therefore expected inducing the initial stage of scaling on the RO membranes. For instance, once the Co^{2+} concentration exceeds 10 mM (only around two times of the concentration in the feed solution), colloidal $Co(OH)_2$ would appear under neutral and alkaline environments (Fig. 3a). In addition to Cu^{2+}, copper ions would mainly present as $CuOH^+$ and tenorite (CuO) species in all pH environments due to their high formation constants (−7.49 and −7.73) when Cu^{2+} concentration exceeding 1 μM (Fig. 3b). This clearly points out that thermodynamically speaking, there would be a significant amount of CuO species in our system (Cu^{2+} concentration in our system was ~0.22 mM). Importantly, a vast amount of Fe^{3+} ions would present as hematite species once the Fe^{3+} concentration is greater than 0.1 μM (Fig. 3c). This threshold concentration is almost three orders of magnitude lower than the Fe^{3+} concentration in our studied system. Similar to cobalt ions, ZnO colloids would initiate to precipitate when pH arises to neutral environment but then slightly disappears because of the formation of $Zn(OH)_3^-$ and $Zn(OH)_4^{2-}$ at high pH environment (Fig. 3d).

Based on our aqueous chemistry calculation, the development of surface scalants are likely initiated by the deposition of metal hydroxide under alkaline environment. As the scalants growing and gradually blocking the pores of the membrane, most elements would not be able to penetrate through the membrane anymore and as a result they were concentrated on the surface of the RO membrane. Importantly among these elements, Fe and Cu are particular prone to develop metal hydroxide colloids even in the acidic environment as long as their concentrations exceed 0.1 and 1.0 μM, respectively. At the same time, the concentration polarization taking place at the membrane surface would further enhance the Fe and Cu concentration near the membrane surface. By this manner, the formation and deposition of Cu/Fe hydroxide colloids could be initiated and thus block the pores of RO membranes. On the other hand, despite the concentrations of other elements such as Mn^{2+} and Cr^{2+} did not exceed their corresponding threshold concentration of the formation of metal hydroxide, they are likely to be adsorbed by Cu/Fe hydroxide because the later two have high affinity toward the formers. Indeed, particularly the iron hydroxide, is the most important mineral controlling the transport of hazardous pollutant elements in the natural environment [31–33]. As a result, the formation of Cu/Fe hydroxide together with afterwards adsorption behaviors is thus likely accounting for the observed scaling phenomenon.

We further converted observed results into the bar graphs as shown in Fig. 4. The brightest region indicates the place where the scalants were highly deposited. Such bar graphs can provide a straightforward vision of the vertical distribution of each element beneath the membrane surfaces. In a good agreement with results shown in Fig. 2, it is obvious that most elements were particularly concentrated at a few micrometers beneath the surface of RO membranes.

3.2. Interpretation of flux decline by classic fouling models and a two-phase fouling model

Fig. 5 shows the experimental results of permeate flux during 24 h of continuous filtration. Simulation results of the flux decline curves, which are based on the four fouling models given by Eqs. (2)–(5), are also shown in Fig. 5. Correlations (R^2) between the fitting results and the experimental data are used to evaluate the goodness of fitting. As shown in Fig. 5a, none of the four classical models were capable of appropriately fitting the permeate flux

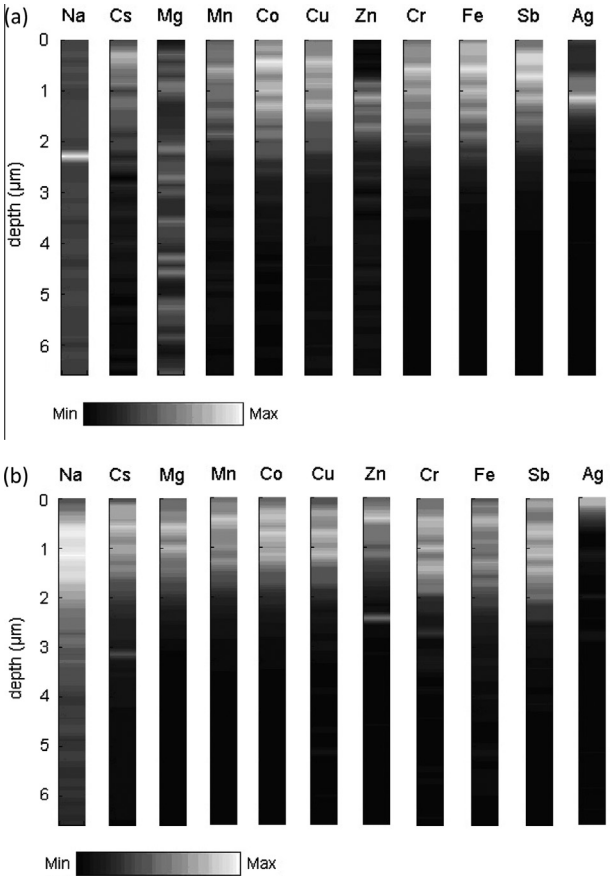

Fig. 4. Vertical distributions of scalants within the RO membrane: (a) at pH 4; (b) at pH 9. The data set presented herein was the one closest to the average values.

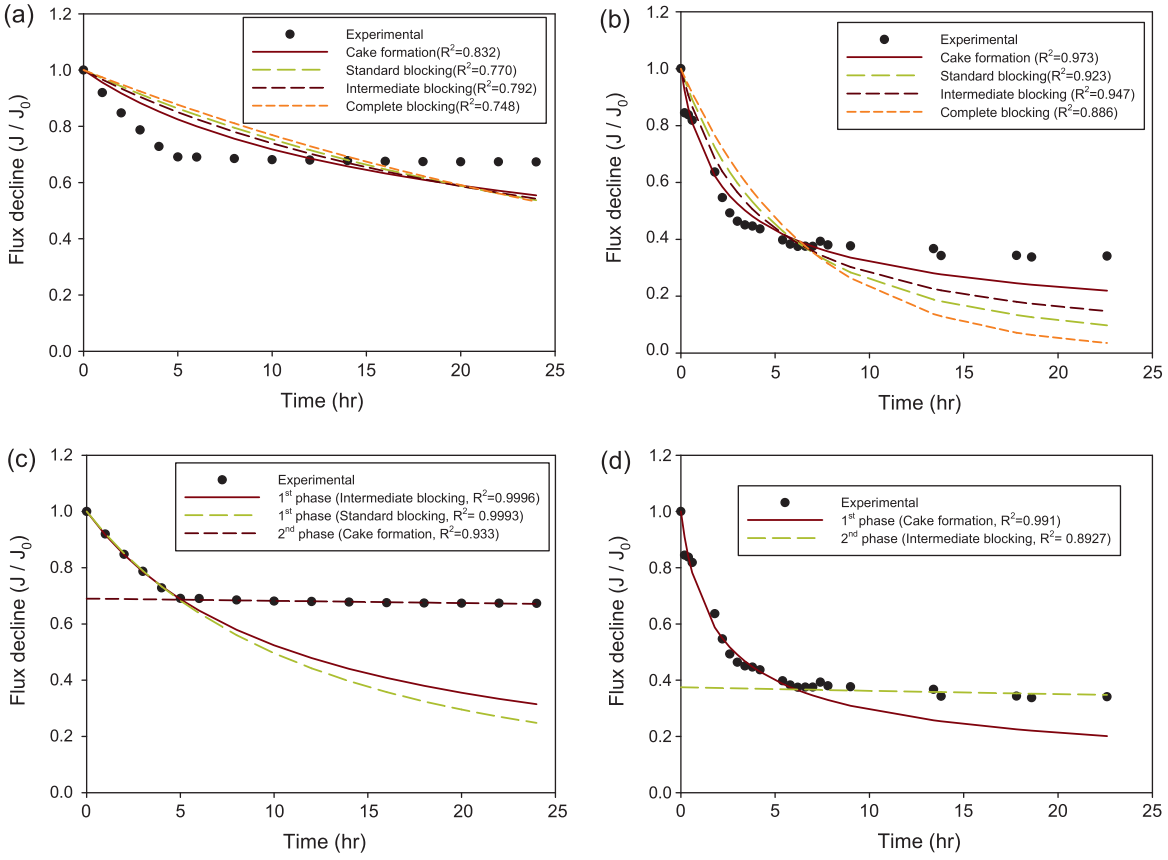

Fig. 5. Experimental results of permeate flux decline curves and simulated curves of the classical fouling models at (a) pH 4; (b) pH 9; two-phase modified fouling model at (c) pH 4; (d) pH 9. The relative standard deviations of these experiment data are <5%.

decline under acidic conditions (pH 4). The highest correlation coefficient observed is only 0.832 (cake formation model). Observed low correlation coefficient is mainly attributed to the poor fitting at the flux variation after 5 h of filtration. This means none of these fouling models alone could provide a possible physical insight behind the observed fouling behaviors. Alternatively, as suggested in the literature [34,35], one might probably divide the experimental data sets into two distinct parts, i.e., an early and a late stage period. By this manner, a two-phase fitting approach describing each filtration period separately could successfully fit experimental results very well as shown in Fig. 5c and d. In the case as shown in Fig. 5c, the flux variation in the initial stage (0–5th hour) can be well described either by the intermediate blocking or the standard blocking models as indicated by the excellent regression coefficients (R^2 = 0.9996 and 0.9993, respectively). In the second stage (after 5th hour), the flux variation seems to reach a steady state and could be well described by the cake-formation model (R^2 = 0.933). This means the aggregation of scalants and afterwards deposition of aggregates onto the membrane surface are the dominant mechanisms accounting for the observed flux variation. Once a layer of cake-like scaling has developed, the cake formation became the dominant mechanism in the following stage. In other words, in this stage all pores have already been fully blocked by the scalants so that no more significant flux variation would be observed. Further, as suggested in Figs. 2 and 3, these scalants are likely the colloids of iron and copper hydroxides.

In contrast to the filtration under acid condition, the flux variation under the alkaline condition (pH 9) was fitted relatively much better by the four classic fouling models (Fig. 3b). From this point of view, the mechanisms including cake-formation, standard blocking, and intermediate blocking seem to involve in the observed flux drop (all of them exhibit $R^2 > 0.9$). In other words, an abundant amount of metal hydroxide colloids would deposit on the particles that have already blocked the pores, precipitated on other particles to form multilayer scalants, and adsorbed onto the pore walls. Importantly, in a good agreement with observations shown in Figs. 2 and 4, these metal hydroxides were mainly depositing onto the membrane surface instead of penetrating into the RO membrane. Obviously, the two-phase modeling approach would reach a much better correlation coefficient as shown in Fig. 5d. Based on fitting results, it is suggested that the flux drop under alkaline environment could be attributed to the cake formation in the first five hours following by the gradually development of intermediate blocking. In other words, an abundant amount of metal hydroxide colloids were precipitating and depositing onto the membrane surface in the first 5 h, leading to the formation of a cake layer (cake formation). Once the cake layer has fully developed, the scaling kept growing and gradually blocking the entire membrane surfaces (intermediate blocking).

4. Conclusions

In this study, the vertical distributions of LLW relevant elements in the scalants were profiled by LA-ICP-MS. It is found that most scalants would deposit on the depth of first few micrometers below the RO membrane surface. Following aqueous chemistry calculation suggested surface concentration polarization might induce the formation of iron, copper, zinc and cobalt hydroxide colloids and they are likely attributed to the formation of surface scalants. Fitting experimental results with two-phase Hermia's model indicated that the intermediate and standard blocking mechanisms

were accounting for the development of scaling in the first five hours of filtration, following by the cake formation mechanism throughout the entire filtration period under the acid environment. In contrast under the alkaline condition, the cake formation was first developing in the first five hours while the intermediate blocking mechanism was responsible for the following scaling growing behaviors.

Acknowledgment

Financial supporting to a research project (NSC 100-2221-E-033-010) from National Science Council Taiwan is acknowledged.

References

[1] S. Shirazi, C.-J. Lin, D. Chen, Inorganic fouling of pressure-driven membrane processes — a critical review, Desalination 250 (2010) 236–248.
[2] A. Antony, J. Low, S. Gray, A. Childress, P. Le-Clech, G. Leslie, Scale formation and control in high pressure membrane water treatment systems: a review, J. Membr. Sci. 383 (2011) 1–16.
[3] T. Waly, M.D. Kennedy, G.-J. Witkamp, G. Amy, J.C. Schippers, The role of inorganic ions in the calcium carbonate scaling of seawater reverse osmosis systems, Desalination 284 (2012) 279–287.
[4] S.F.E. Boerlage, M.D. Kennedy, I. Bremere, G.J. Witkamp, J.P. van der Hoek, J.C. Schippers, The scaling potential of barium sulphate in reverse osmosis systems, J. Membr. Sci. 197 (2002) 251–268.
[5] N.H. Lin, W.-Y. Shih, E. Lyster, Y. Cohen, Crystallization of calcium sulfate on polymeric surfaces, J. Colloid Interf. Sci. 356 (2011) 790–797.
[6] Ch. Tzotzi, T. Pahiadaki, S.G. Yiantsios, A.J. Karabelas, N. Andritsos, A study of $CaCO_3$ scale formation and inhibition in RO and NF membrane processes, J. Membr. Sci. 296 (2007) 171–184.
[7] A.J. Karabelas, M. Kostoglou, S.T. Mitrouli, Incipient crystallization of sparingly soluble salts on membrane surfaces: the case of dead-end filtration with no agitation, Desalination 273 (2011) 105–117.
[8] G. Zakrzewska-Trznadel, M. Harasimowicz, A.G. Chmielewski, Membrane processes in nuclear technology-application for liquid radioactive waste treatment, Sep. Purif. Technol. 22–23 (2001) 617–625.
[9] A.K. Pabby, Membrane techniques for treatment in nuclear waste processing: global experience, Membr. Technol. 11 (2008) 9–13.
[10] R.D. Ambashta, M.E.T. Sillanpää, Membrane purification in radioactive waste management: a short review, J. Environ. Radioact. 105 (2012) 76–84.
[11] D. Rana, T. Matsuura, M.A. Kassim, A.F. Ismail, Radioactive decontamination of water by membrane processes — a review, Desalination 321 (2013) 77–92.
[12] Radioactive colloid removal by optimizing chemical parameters. In EPRI TR-1003232, 2003.
[13] T.H. Chong, F.S. Wong, A.G. Fane, Fouling in reverse osmosis: detection by non-invasive techniques, Desalination 204 (2007) 148–154.
[14] R. Chan, V. Chen, Characterization of protein fouling on membranes: opportunities and challenges, J. Membr. Sci. 242 (2004) 169–188.
[15] T.H. Wang, M.-C. Huang, Y.-K. Hsieh, W.-S. Chang, J.-C. Lin, C.-H. Lee, C.-F. Wang, Influence of sodium halides (NaF, NaCl, NaBr, NaI) on the photocatalytic performance of hydrothermally synthesized hematite photoanodes, ACS Appl. Mater. Interf. 5 (2013) 7937–7949.
[16] J. Koch, D. Günther, Review of the state-of-the-art of laser ablation inductively coupled plasma mass spectrometry, Appl. Spectrosc. 65 (2011) 155A–162A.
[17] S. Peng, Q. Hu, R.P. Ewing, C. Liu, J.M. Zachara, Quantitative 3-D elemental mapping by LA-ICP-MS of a basaltic clast from the hanford 300 area, Washington, USA, Environ. Sci. Technol. 46 (2012) 2025–2032.
[18] Y.-K. Hsieh, H.-A. Hsieh, H.-F. Hsieh, T.H. Wang, C.-C. Ho, P.-P. Lin, C.-F. Wang, Using laser ablation inductively coupled plasma mass spectrometry to characterize the biointeractions of inhaled CdSe quantum dots in the mouse lung, J. Anal. At. Spectrom. 28 (2013) 1396–1401.
[19] T.H. Wang, C.-H. Jian, Y.-K. Hsieh, F.-N. Wang, C.-F. Wang, Spatial distributions of inorganic elements in honeybees (*Apis mellifera* L.) and possible relationships to dietary habits and surrounding environmental pollutants, J. Agric. Food Chem. 61 (2013) 5009–5015.
[20] T.H. Wang, H.-A. Hsieh, Y.-K. Hsieh, C.-S. Chiang, Y.-C. Sun, C.-F. Wang, The fate and in vivo biodistribution of CdSe quantum dots in rat tissues: a laser ablation inductively coupled plasma mass spectrometry study, Anal. Bioanal. Chem. 404 (2012) 3025–3036.
[21] L.-S. Chen, T.H. Wang, Y.-K. Hsieh, C.-H. Hsu, J.C.-T. Lin, C.-F. Wang, Visualization of clogs developed from interaction between APDC and low-level radwaste relevant nuclides on RO membranes: a LA-ICP-MS study, J. Membr. Sci. 456 (2014) 202–208.
[22] C. Jarusutthirak, S. Mattaraj, R. Jiraratananon, Influence of inorganic scalants and natural organic matter on nanofiltration membrane fouling, J. Membr. Sci. 287 (2007) 138–145.
[23] F. Wang, V.V. Tarabara, Pore blocking mechanisms during early stages of membrane fouling by colloids, J. Colloid Interf. Sci. 328 (2008) 464–469.
[24] Y.-L. Cheng, D.-J. Lee, J.-Y. Lai, Filtration blocking laws: revisited, J. Taiwan Inst. Chem. Eng. (2010) 45.
[25] C. Tien, B.V. Ramarao, Revisiting the laws of filtration: An assessment of their use in identifying particle retention mechanisms in filtration, J. Membr. Sci. 383 (2011) 17–25.
[26] C.Y. Tang, T.H. Chong, A.G. Fane, Colloidal interactions and fouling of NF and RO membranes: A review, Adv. Colloid Interface Sci. 164 (2011) 126–143.
[27] M. Kostoglou, A.J. Karabelas, On modeling incipient crystallization of sparingly soluble salts in frontal membrane filtration, J. Colloid Interf. Sci. 362 (2011) 202–214.
[28] J. Hermia, Constant pressure blocking filtration law application to power law non-Newtonian fluids, Trans. Inst. Chem. Eng. 60 (1982) 183–187.
[29] Gnuplot program, <http://www.gnuplot.info/> (access 25.03.13).
[30] W.D. Schecher, D.C. McAvoy, MINEQL+: A Chemical Equilibrium Modeling System, Version 4.5 for Windows, User's manual, v2.00, Environmental Research Software, Hallowell, Maine, 2003.
[31] Y.-L. Jan, T.H. Wang, M.-H. Li, S.-C. Tsai, Y.-Y. Wei, S.-P. Teng, Adsorption of Se species on crushed granite: a direct linkage with its internal iron-related minerals, Appl. Radiat. Isot. 66 (2007) 14–23.
[32] T.H. Wang, C.-L. Chen, L.-Y. Ou, Y.-Y. Wei, F.-L. Chang, S.-P. Teng, Cs sorption to potential host rock of low-level radioactive waste repository in Taiwan: experiments and numerical fitting study, J. Hazard. Mater. 192 (2011) 1079–1087.
[33] D.A. Dzombak, F.M.M. Morel, Surface Complexation Modeling: Hydrous Ferric Oxide, Wiley-Interscience, New York, 1990.
[34] J. Ho, S. Sung, Effects of solid concentrations and cross-flow hydrodynamics on microfiltration of anaerobic sludge, J. Membr. Sci. 345 (2009) 142–147.
[35] A. Charfi, N. Ben Amar, J. Harmand, Analysis of fouling mechanisms in anaerobic membrane bioreactors, Water Res. 46 (2012) 2637–2650.